Draft version September 29, 2016
Preprint typeset using LaTeX style AASTeX6 v. 1.0

arXiv:1609.08711v1 [astro-ph.SR] 27 Sep 2016

HIGHLY VARIABLE YOUNG MASSIVE STARS IN ATLASGAL CLUMPS

M. S. N. Kumar
Centre for Astrophysics Research, University of Hertfordshire, Hatfield, AL10 9AB, UK
Instituto de Astrofísica e Ciências do Espaco, Universidade do Porto, CAUP, Rua das Estrelas, 4150-762 Porto, Portugal

C. Contreras Peña
Centre for Astrophysics Research, University of Hertfordshire, Hatfield, AL10 9AB, UK

P. W. Lucas
Centre for Astrophysics Research, University of Hertfordshire, Hatfield, AL10 9AB, UK

M. A. Thompson
Centre for Astrophysics Research, University of Hertfordshire, Hatfield, AL10 9AB, UK

ABSTRACT

High-amplitude variability in Young Stellar Objects (YSOs) is usually associated with episodic accretion events. It has not been observed so far in massive YSOs. Here, the high-amplitude variable star sample of ContrerasPeña et al.(2016) has been used to search for highly-variable(ΔK$\geq$1 mag) sources coinciding with dense clumps mapped using the 850μm continuum emission by the ATLASGAL survey. 18 variable sources are centred on the sub-mm clump peaks, and coincide ($<1''$) with a 24μm point or compact ($<10''$) source. 13 of these 18 sources can be fit by YSO models. The 13 variable YSOs(VYSO) have luminosities of $\sim10^3$ L$_\odot$, an average mass of 8 M$_\odot$ and a range of ages up to 10^6 yr. 11 of these 13 VYSOs are located in the midst of infrared dark clouds. 9 of the 13 sources have ΔK$>$2 mag, significantly higher compared to the mean variability of the entire VVV sample. The light curves of these objects sampled between 2010-2015 display rising, declining, or quasi-periodic behaviour but no clear periodicity. Light-curve analysis using Plavchan method show that the most prominent phased signals have periods of a few hundred days. The nature and time-scale of variations found in 6.7 Ghz methanol maser emission (MME) in massive stars are similar to that of the VYSO light curves. We argue that the origin of the observed variability is episodic accretion. We suggest that the timescale of a few hundred days may represent the frequency at which a spiralling disk feeds dense gas to the young massive star.

Keywords: Stars:formation — stars:massive — stars:variability Herbig Ae/Be

1. INTRODUCTION

Variability studies of young low mass stars, both in the line and continuum, have proven to be powerful tools to decipher the physics of star formation and pre-main-sequence evolution. Low mass Young Stellar Objects (YSOs) displaying optical/infrared flux variability trace a variety of phenomena (Carpenter et al. 2001; Fernandez & Eiroa 1996) such as accretion events in the disk, magnetospheric activity (Bouvier, et al. 2007), spots (Bouvier & Bertout 1989) and flares on the stellar surface. High-amplitude variability is often associated with episodic events of accretion, well-known through objects such as FUors (named after FU Orionis) and EXors (named after EX Lupi). Hence, they are excellent laboratories to understand the accretion phenomenon, especially at unresolved spatial scales representing the accretion disk and the young star.

Higher mass young stars are elusive objects that spend their brief youth while deeply embedded in extremely dense molecular cores. Optical photometric variability studies of Herbig Ae/Be stars (intermediate mass YSOs) concluded that large amplitude variability is confined to stars with spectral types later than B8 (Herbst &

Shevchenko 1999). This result should not be surprising, considering that stars more massive than 8 $M_\odot$ would lack a pre-main-sequence phase appearing directly on the zero-age-main-sequence (Hayashi 1966; Iben 1965). In other words, optically visible intermediate and massive stars should have already arrived on the zero-age-main-sequence (Bernasconi & Maeder 1996) with very little episodic accretion activity. Moreover, once a massive star becomes optically visible, the accretion rates are low (Hartmann, Kenyon & Calvet 1993) and the accretion luminosity itself is insignificant compared to the total luminosity. On the other hand, the infrared counterparts (*IRcs*) to high-mass protostellar objects (*HMPO*) (Kumar & Grave 2007; Grave & Kumar 2009), represent some sort of a pre-main-sequence phase for the massive stars because these objects are deeply embedded in their natal dense molecular cores, show high accretion rates, and they are detected only in the infrared bands. Hence, they are more likely to display variability associated with accretion episodes. However, a systematic search for variability in such objects is still lacking. *IRcs* to *HMPO*'s are often visible as point-sources in the near-infrared K-band in the midst of dark clouds. The following work is an attempt to find variability in such sources.

The Vista Variables in the Via Lactea survey (VVV, Minniti et al. 2010) provides $ZYJHK_s$ photometry of ≈ 560 deg^2 of the Galactic Bulge and the adjacent midplane. In addition, the survey has yielded ≈ 50 to 70 epochs of K_s photometry over a period of 5 years. The VVV survey covers much of the Galactic fourth quadrant, which is known for its intense activity of high-mass star formation in the Milky-Way. This virtue of the fourth quadrant has caused it to be the focus for several other Galactic plane surveys such as ATLASGAL (Schuller et al. 2009) and HiGal (Molinari et al. 2010), aiming to uncover deeply embedded high-mass stars and cluster forming cores. The ATLASGAL survey has provided an unbiased data set of dense molecular clumps. These are massive clumps, often associated with high-mass star formation. Prior to the VVV study, no eruptive variable YSOs were known with luminosities higher than a few hundred solar luminosities (Audard et al. 2014). In this work we inspect the VVV sample of 816 high amplitude infrared variable stars discovered by Contreras Peña et al. (2016a) and we isolate variables that coincide with ATLASGAL clumps in an effort to find variable young intermediate/high-mass stars.

2. HIGH-AMPLITUDE VARIABLE STARS WITHIN ATLASGAL CLUMPS

The sample of high-amplitude ($\Delta K_s > 1$ mag) variable stars uncovered from the VVV survey has been described by Contreras Peña et al. (2016a). They found 816 variable stars in the 4th Galactic quadrant (l=295° to 350°, b= -1.1° to 1.0°). The identification method and the selection criteria are detailed in Contreras Peña et al. (2016a). Here, the interest is to find variable stars that are *IRcs* to *HMPO*'s. By definition an *HMPO* should be associated with a massive molecular clump, typical of the ATLASGAL clumps. The 816 high-amplitude variable stars were matched with a radius of 300″ to all the peak positions listed in the ATLASGAL web database, resulting in 39 matched sources. To ensure that the matched variable star actually represents a luminous (massive) source with infrared excess (young star), rather than an unrelated foreground or background source, we used the following constraints in the next step of filtering. The ATLASGAL data has an angular resolution of 19.2″, and the pointing rms better than 4″. The variable star associated with the sub-mm clump (almost always within the peak of the 19.2″beam) must coincide (to better than 1″) with a 24μm source that is either point or compact (<10″) like. 18 of the 39 stars above satisfied these criteria. Next, the spectral energy distribution (SED) of the source should be representative of a YSO and not a stellar photosphere. Therefore, the 1μm –850μm photometric measurements for these 18 objects were assembled using any, and all available data from the 2MASS, GLIMPSE, MIPSGAL, WISE, HiGal and the ATLASGAL databases (See Sec. 3 and Table 2). The resulting SEDs were fitted using the SED fitting tool described by Robitaille et al. (2007) which attempts to model the observed SED with an appropriate young stellar object model, at the same time checking if the SED can represent a main-sequence photosphere. Five of the 18 objects were fitted by stellar photospheres, leaving 13 VVV sources that were fit with YSO models. These 13 variable young stellar objects (VYSOs) are listed in Table 1 along with their known properties.

In Table 1, σK_s is the typical scatter in each magnitude bin of K_s for a given VVV tile (see Contreras Peña et al. (2016a) for a full description). This scatter is in the range 0.4-0.6 mag as is typical with uncorrected pipeline photometry of the VVV tiles. The choice of $\Delta K_s > 1$ mag cut-off (both in this work and that of Contreras Peña et al. 2016a), is a conservative choice to select objects well above the scatter σK_s. This choice is the reason why only a small number of 13 VYSOs are found in this study. An extended study is underway to examine the general variability characteristics of high-mass YSOs by employing the relatively accurate, paw-print photometry that displays lower scatter levels.

Fig. Set 1. VYSO colour overlays

To visualise and examine the environment of the VYSOs, we composed colour images using the Spitzer MIPSGAL (Carey et al. 2009) and GLIMPSE (Church-

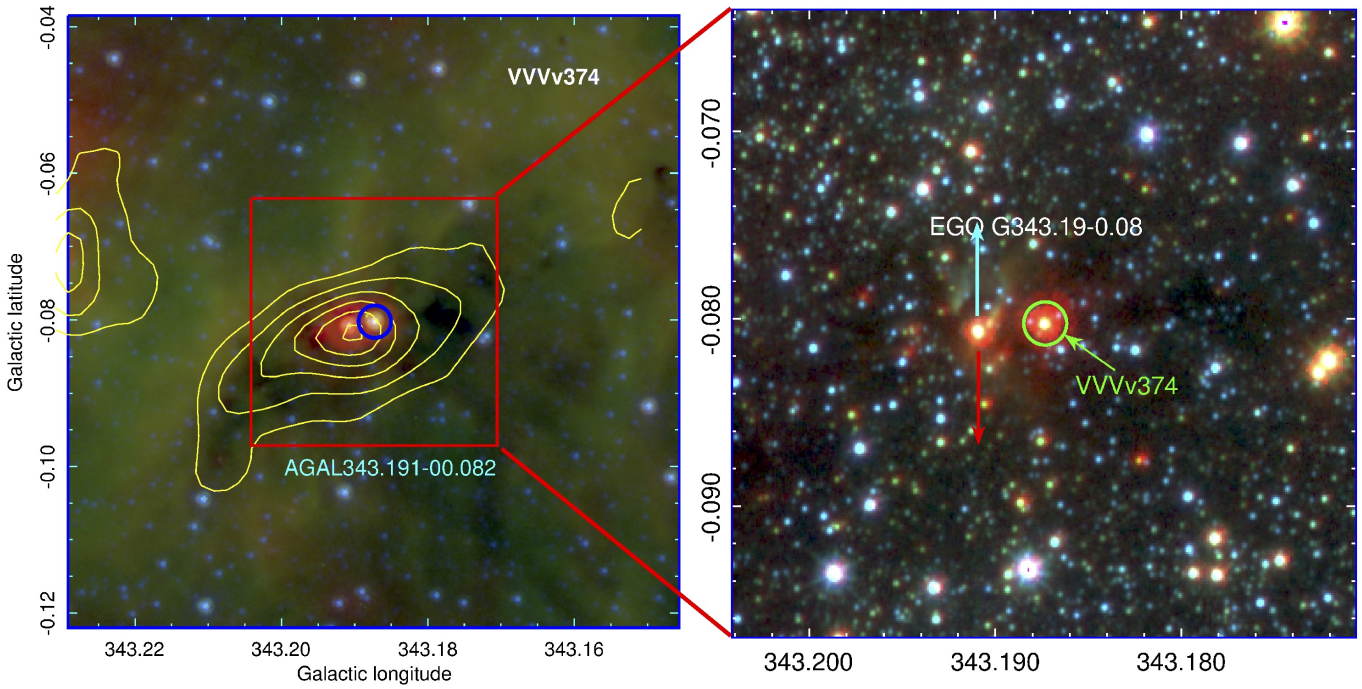

Figure 1. The environment of VVVv374. Left Panel: Spitzer-MIPS 24μm , IRAC 8μm and 3.6μm images are coded as red, green and blue respectively to compose the colour image which reveal the infrared dark filament/cloud. Yellow contours show the 870μm emission (starting at 0.1 Jy, in steps of 0.1 Jy) from the ATLASGAL data tracing the molecular clump associated with the infrared dark cloud. Two young stars are visible at the peak of the clump. The blue circle identifies the variable young star. Right Panel: Zoom in view of the two young stars shown with a colour composite of the Spitzer-IRAC 4.5μm VVV K_s and VVV H-band images coded as red, green and blue respectively. The young star adjacent to the variable source is associated with an extended green object (EGO) as shown. Blue and red arrows represent possible blue and red shifted lobes of the outflow associated with the EGO.

well et al. 2009) cutouts and overlaid contours of 850μm emission from the ATLASGAL data. In Figure. 1(left panel) we display such an overlay for the source VVVv374. It is an excellent example of the 13 objects listed in Table 1. The Spitzer MIPS 24μm , IRAC 8μm , and IRAC 3.6μm images are red, green and blue respectively, and the yellow contours show the ATLASGAL 850μm emission. Similar plots for the remaining 12 targets are shown in the supplementary Fig. Set 1. In Figure. 1(left panel) the infrared VYSO appears as a bright 24μm source, embedded inside the elliptical shaped dense core traced by the 850μm emission contours. The dark patch in the background image reveals the associated infrared dark cloud. In 11 of the 13 cases, the ATLASGAL cores are associated with a catalogued infrared dark cloud (IRDC) (Peretto & Fuller 2009). The presence of an IRDC is an important signpost that the selected objects are indeed sites of massive star formation. The star formation activity in VVVv374 is further evident through the presence of an extremely green object EGO (Cyganowski et al. 2008). The right panel in Figure. 1 shows this feature for VVVv374, highlighting the bipolar outflow traced by the EGO. Here the IRAC4.5μm , VVV K and H band images are used as red, green and blue respectively. The Vizier database was used to search a 30″ radius around each target to find known sign-posts of star formation such as IRDCs, EGOs, Masers, and HII regions and they are listed in the last column of Table 1.

We note that 9/13 sources in Table 1 have amplitudes $\Delta K_s > 2$ mag, which is significantly higher than the mean variability of all the YSOs in the VVV sample of Contreras Peña et al. (2016a), regardless of the light curve classification. In that study, high amplitude was found to be correlated with an early stage of evolution, as traced by the 2 to 22 μm spectral index. The presence of ATLASGAL cores and IRDCs tends to support this correlation, in addition to indicating that high amplitude variable YSOs can be massive systems.

3. SED FITTING

By using the SED modelling, one can qualitatively assess the luminosity and mass of the stars of interest. The photometric data compiled for the 13 objects is tabulated in Table 2. It includes the four Spitzer-IRAC bands from the GLIMPSE survey (3.6μm , 4.5μm , 5.8μm , 8μm), two bands from the WISE survey (12μm , 22μm), Spitzer-MIPS photometry at the 24μm band (Robitaille et al. 2008), 5 bands from the Herschel-HiGal survey (70μm , 170μm , 250μm , 350μm , 500μm) and the ATLASGAL 850μm band. Whenever MIPS

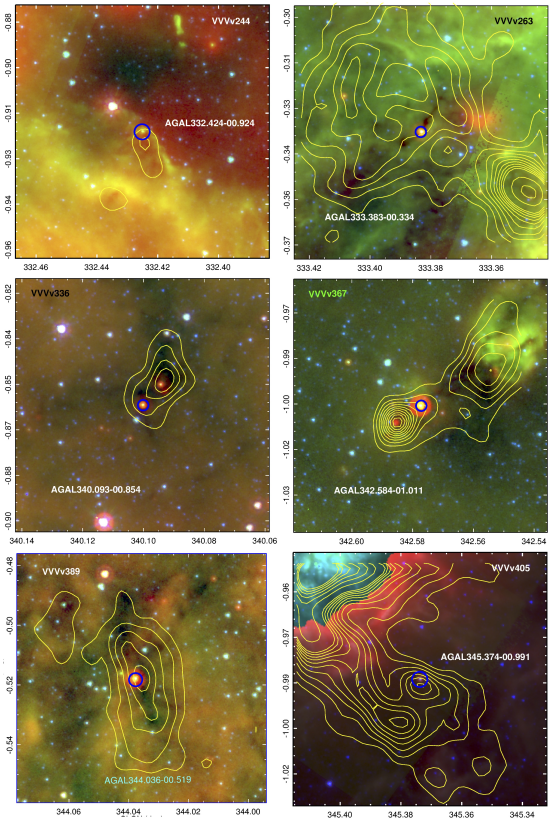

Figure 1. Same as left panel of Fig.1

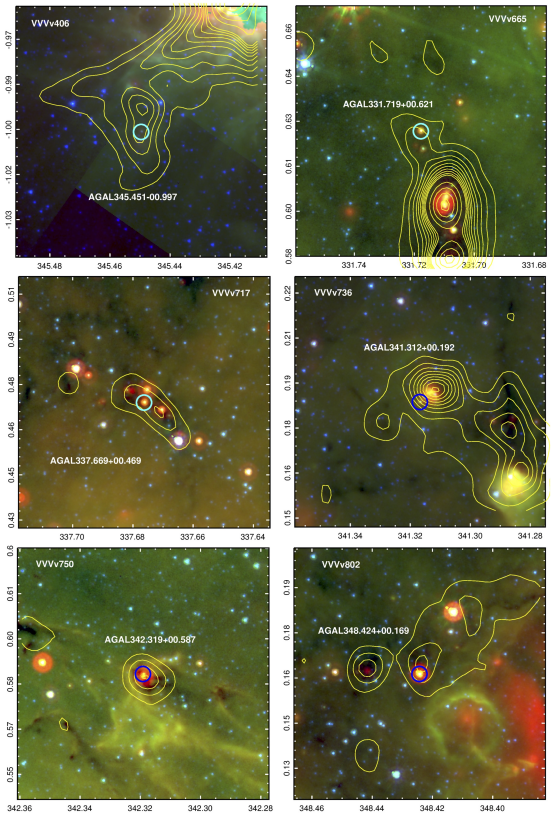

Figure 1. Same as left panel of Fig.1

24μm photometry is available the WISE 22μm is ignored to ensure using the higher quality data. Given that our targets display >1 mag variation in the K band, and the above surveys are non-contemporaneous, the variations in the near-infrared J and H bands are expected to be of similar amplitude. Therefore they are not used to model the SEDs. In the IRAC 3.6μm and 4.5μm bands, typically 0.2-0.4 mag variations are reported for low mass YSOs (Faesi et al. 2012; Wolk et al. 2015). Moreover Contreras Peña et al. (2016a) typically find lower amplitude variability at these longer wavelengths compared to K-band variation. Such variations should not affect the overall SED and the resulting fit.

The photometric data listed in Table 2 was fed to the SED fitting tool (Robitaille et al. 2007). The physics of YSOs behind this tool is detailed in Robitaille et al. (2006). We used appropriate apertures for each band, a classification as data or upper limit, and a range in distance and extinction for each source. The apertures used are 4″ for Spitzer-IRAC and 12″ for WISE bands and 6″diameter for MIPS 24μm , respectively. The full-width half maximum of the HiGal and ATLASGAL cores were used as aperture diameters for the sub-mm data.

The data at wavelengths shorter than (and inclusive of) 24μm were employed as "data points" (as they critically define the fitted models), and the remaining longer wavelength data are set as "upper limits" (which allow to constrain the fitted models) in the SED fitting (e.g. Grave & Kumar 2009). This choice is made to minimise the contamination from other sources enclosed within the large beams of the long wavelength data. The SED fitting tool scales and fits YSO models derived from a library of 200000 models. The scaling is done by adopting an appropriate combination of extinction and distance within a range provided by the user. Neither of these factors are known with certainty (see Contreras Peña et al. 2016a) for our sources, so, we used a fixed range of A_v=5–50mag and d=1–13kpc for all 13 objects. Typically, the adopted choice of the SED fitter is correct within a factor of two for both values because of the logical combination of YSO models stored in the library. The choice of A_v and the distance used by the SED fitter is an output from the fitting results, listed in Table 3 along with other parameters. We note that IRDCs in quadrant 4 are typically located at distances of ∼3 kpc (Jackson et al. 2008), and distances over ∼8 kpc are unlikely because these dense clouds require a bright mid-infrared background in order to be observed in silhouette. The SED fitting results are consistent with the expected locations on the near side of the Milky Way.

The fitting procedure is based on χ^2 minimisation method and yields a best fit model together with a range of models satisfying the criteria ${\chi^2}_{best} - \chi^2$ per data

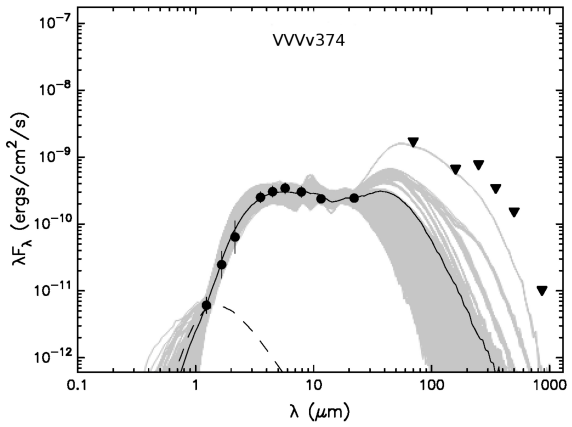

Figure 2. SED fitting results for the source VVVv374. Filled circles and triangles show the "data points" and "upper limits" respectively. Solid black line and grey lines show the best fit model and the models satisfying the criteria $\chi^2_{best} - \chi^2 < 3$ respectively. The dashed line represents the embedded photosphere of the best fit YSO model.

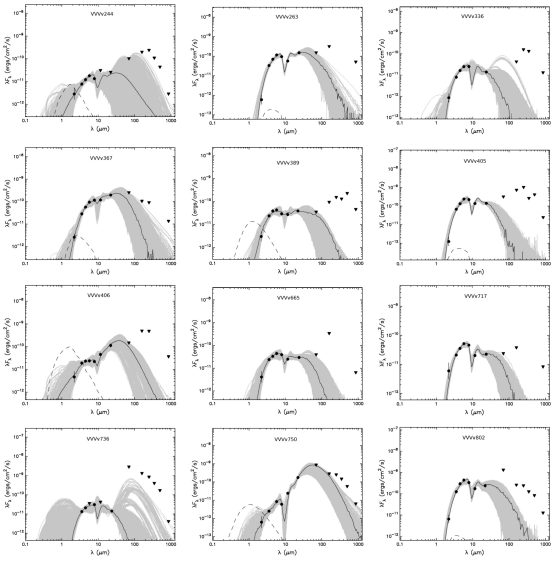

Figure 2. Same as Fig.2

point is less than 3. The model parameters listed in Table 3 are weighted means of this suite of models, the weights being the inverse of the χ^2 of each model. In Table 3 the column N_{fits} indicate the number of models used to compute the parameters satisfying the above criteria, and N_{fits2} are the number of models which has a non-zero value of envelope accretion rate. The fitted YSO models for the exemplar source VVVv374 is shown in Figure. 2. The remaining fits are displayed in the supplementary Fig. Set 2.

Fig. Set 2. SED models for VYSOs

3.1. *SED fitting results*

The most reliable output of the SED fitting procedure is the luminosity because they are obtained by a simple scaling of the pre-computed radiation transfer models to match the flux peak and shape of the observed SED by using an appropriate combination of extinction and distance to minimise the χ^2 (Robitaille et al. 2007). This is also the reason why the extinction and distance estimates given by the fitting procedure turn out to be correct within a factor of two. This procedure will select optimal combinations of mass and age to match the observed SED from an uniformly sampled parameter space (see Robitaille et al. 2006) which is used to derive the temperature and radius of the young star through evolutionary models. From Table. 3 it can be seen that the selected high-amplitude variable stars are best modelled as intermediate to high mass objects with an average luminosity of 10^3 $M_\odot$, and mass of 8 $M_\odot$.

The modelled ages show that they are typically million year old objects, with a significant level of disk and envelope accretion rates. The number of models N_{fits2} with a non-zero envelope accretion rate are fewer compared to the total number of models, because much of the longer wavelength data are used as upper limits, to avoid contribution from adjacent sources. However, in 9/13 sources the HiGal 70μm datum corresponds to an unresolved source detected within 5″of the VVV source. Since the Herschel/PACS beam size is 6″ × 12″ at this wavelength, this strongly implies that the 70μm flux arises in the disk or envelope of the YSO, rather than the larger scale cloud. If we were to use the 70μm data for these 9 sources actively in the fit, instead of upper limits, at least 6/13 sources would be fitted with a non-zero envelope accretion rate, compared to the 2/13 sources in Table 3. Consequently, it appears likely that these YSOs have a range of ages extending below one million years. We also note that using HiGal fluxes as data points instead of upper limits would tend to increase the total luminosity of these systems.

The 13 targets are all near-infrared visible, suggesting that they have partially emerged from the deeply embedded phase which is often captured only at sub-mm regime. The inferred disc accretion rates represent a mean value of 10^{-6} $M_\odot\,yr^{-1}$. It is two orders of magnitude smaller than the high disk accretion rates measured through millimeter observations (Cesaroni et al. 2007) or from SED modelling of *IRcs* to *HMPO*'s (Grave & Kumar 2009). The fitting results can be improved by acquiring higher spatial resolution data at longer wavelengths. The results obtained here are merely indicative, the main inference is that the selected targets represent YSOs of high bolometric luminosity, therefore representing massive YSOs.

4. LIGHT CURVES

The VVV data obtained between 2010-2015 have been used to construct the light curves for the 13 sources here. The light curve from the multi-epoch photometric data

for the source VVVv374 is shown in Figure. 3. The remaining light curves are displayed in the supplementary Fig. Set 3. It can be seen that the data points are spread out fairly uniformly along the time axis with several gaps in between, as is typical for the survey observations. The gaps are often larger than one week between consecutive observations but shorter, intra-day time intervals are also sampled. The time series will nearly always detect changes in flux that endure for several months (Contreras Peña et al. 2016a). Regular variations with periods from hours to weeks are also likely to be detected, though one-off variations on these short timescales are likely to be missed. The light curve classifications for these objects from Contreras Peña et al. (2016a), based on the 2010-2015 time series, are listed in Table. 1.

Examining the light curves of all the 13 VYSOs, we do not find visually obvious periodicity, except in the case of VVVv802. This light curve was classified as LPV-Mira by Contreras Peña et al. (2016a), owing to the excellent fit to a sine curve in the 2010-2014 time series. However, the 2015 datum departs from the previous trend. Moreover, the SED of this source (especially the 24μm and 70μm data) does not resemble those of dusty Mira variables discussed by Contreras Peña et al. (2016b), so the Mira interpretation is disfavoured. The observed light curve is the sum of flux variations caused by a variety of phenomena such as accretion, spots, eruptive events, line-of-sight extinction due to rotation of the source (Carpenter et al. 2001). The light curves of some pre-main-sequence stars are shown to have contributions from pulsations (Kallinger, Zwintz & Weiss 2008). Additionally, noise from variable seeing and weather conditions also contribute to the observed light curve. Analysing the light curve with a periodogram can often uncover a phased signal if it happens to be of substantial significance.

Fig. Set 3. SED models for VYSOs

To carry out such analysis, we used the NASA exoplanet archive periodogram tool [1]. This tool offers various algorithms to process both periodic (such as exoplanet or asteroseismic signals) and non-periodic time-series data. The Plavchan method (Plavchan et al. 2008) is most suited to examine non-periodic light curve data. This algorithm uses a phase dispersion minimisation method to detect phased signals by minimising the residuals to phase-folded light curves with a range of possible periods. In using the Plavchan algorithm, the user can adjust values of the number of outlier data points and a phase-smoothing box size. These parameters were

[1] http://exoplanetarchive.ipac.caltech.edu/applications/Periodogram/docs/Algorithms.html

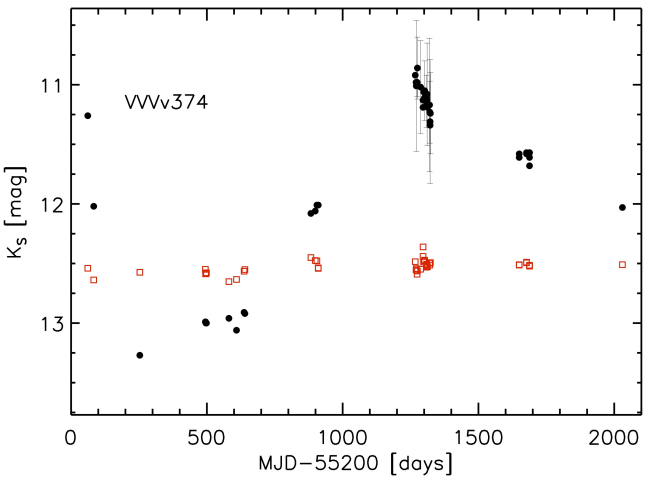

Figure 3. Light curve of the source VVVv374. Red squares show the light curve of a non-varying control object within the same field of view.

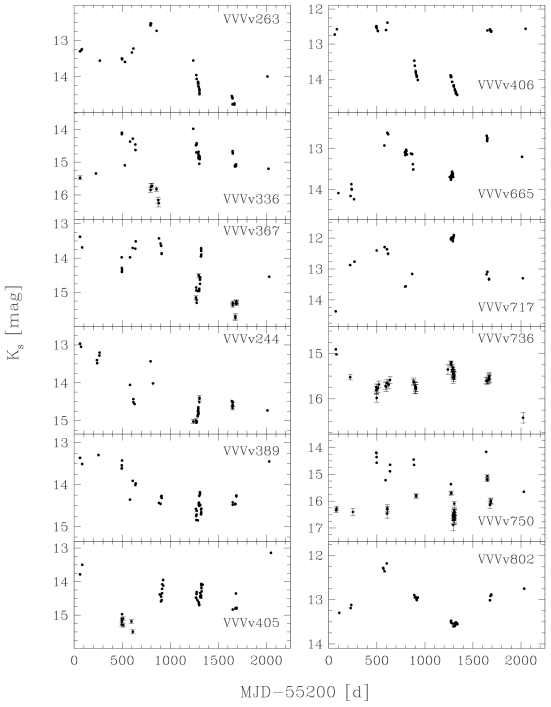

Figure 3. Same as Fig.3

left at default values of 500 and 0.060, which would allow the liberty to reject all data points (maximum 50 for the data here) if no suitable signal was found. On ingesting the light curves to the periodogram tool, it attempts to detect and list phased signals of different frequencies. The signal power is the magnitude of the coefficients in the frequency domain and the probability of obtaining the calculated power for a particular period by chance is given by a p-value. The output is organised to list the most significant periods first, i.e those with the highest signal power and least p-value. P-values are

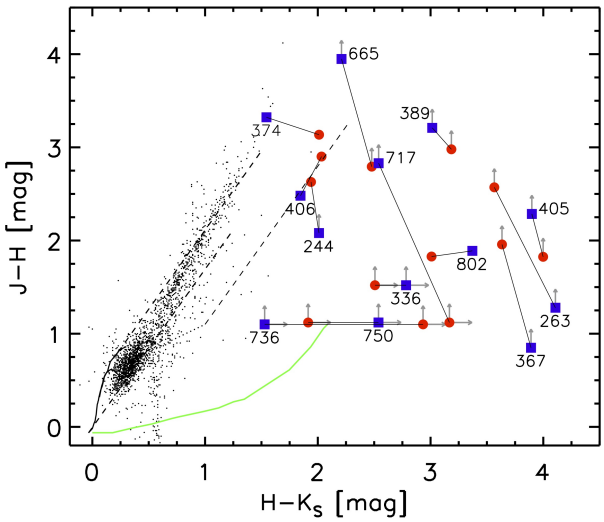

Figure 4. Colour-colour diagram. Black dots are the typical near-infrared colours of stars in a 6′× 6′field centred on the variable sources. The dwarf and giant locus are showed in thick black lines. Dotted line show the T-Tauri locus. Dashed lines enclosing these curves are reddening vectors isolating the reddened groups of those objects. The green curve display the HAeBe locus. The red and blue data points display the colours of each object at the beginning and end of the light curve.

in the range between 0 and 1. The interest here is to detect potential phased signals contributing to the light curve. Therefore, we selected the first three significant periods, which displayed the least p-value, in most cases about four to six orders of magnitude smaller than the p-values of subsequent periods. In other words the first two or three significant periods (with the highest powers) displayed p-values of the order of 10^{-6}–10^{-9} and the subsequent p-values of the order of 10^{-1}–10^{-3} or larger. The most significant periods are listed in Table. 4, where, for each VYSO, the columns Per1, Per2 and Per3 show the periods and the columns Power1, Power2, and Power3 are the respective signal powers. If only two periods Per1 and Per2 are listed for a given source, it means that the power spectrum is relatively clean, lacking further components.

From Table. 4 it is evident that the most significant period (Per1) is of the order of a few hundred days. The median values of Per1, Per2 and Per3 for the 13 sources are 492, 284 and 124 days respectively. Plavchan method is known to be particularly sensitive in producing false peaks at integer multiples of the fundamental period of a real signal, so we compared Per1, Per2, and Per3 for every source in Table 4. There are only limited signs of such an artifact here: some of the periods of the sources VVVv367, VVVv374 and VVVv405 are close to harmonics.

5. NEAR-INFRARED COLOURS

The JHK colour properties of the 13 VYSOs are examined. Multi-band JHK data is available for two epochs, roughly at the beginning and the end of the available light curve baseline. In Figure. 4 we show these two epochs on the J-H vs H-K colour-colour diagram. The first and last epoch are represented by red and blue symbols respectively, joined by a black line. Only three VYSOs are detected in all the three JHK bands at both epochs. The remaining VYSOs have missing detections, either in the J, H, or both, in one or both epochs, owing to the very red nature of these sources. In such cases we have used the VVV sensitivity limits as an upper limit in computing the colours, and they are indicated by the arrows. The VYSOs occupy the reddened HAeBe locus (Lada & Adams 1992) of the colour-colour space. The HAeBe locus encompasses intermediate-massive disk (L_{disk}=0.1 L_{bol}) objects with central holes at $T_D \geq$1000 K. The 13 VYSOs are reddened by different amounts, as evident from the vertical distribution of their location parallel to the reddening vector. In the 5 year timespan, the VYSOs have mostly remained in the HAeBe space, with some variations in reddening. It may be suggestive of infrared excess variations as the cause of photometric variability, although the lack of detections in all the three bands may imply variable reddening as a possible origin.

6. DISCUSSION

In all but one source, the VYSO is offset by <5″ of the ATLASGAL peak. The 850μm peak itself is often associated with a red diffuse (VVVv736, VVVv406) or point source (VVVv374, VVVv336, VVVv367). In the exemplary target VVVv374, the red point source coinciding with the 850μm peak is found to drive an EGO. This feature, that the VYSO is located adjacent to an younger and/or more embedded YSO, may point to a physical association between the two, with some evolutionary lag, the VYSO having formed first. Numerical simulations of high-mass star formation (ex Krumholz et al. 2009) predict such pairs, the younger companion forming due to fragmentation of a Jeans unstable massive disk/envelope. In VVVv263, though the 850μm emission appears diffuse, a high contrast filamentary dark cloud is located in the midst of the emission, and the VYSO is centred at the peak of this infrared filament.

The masses of all 13 VYSOs listed in Table. 3 are in the range 5-11 $M_\odot$, mostly of 7-8 $M_\odot$, representing massive YSO candidates. The distances (from SED models) are in the range 3.5-6.5 kpc, and the internal core extinction is a hundred to few hundred visual magnitudes. Contreras Peña et al. (2016b) have estimated the distance to five of these VYSOs based on radial velocities and/or association with star forming regions. The SED

modelled distances are roughly in agreement with those measurements to better than a factor of two. The models fitted to the source VVVv750 yield an abnormal Av of 450716 mag, and it is the only target with a very young age estimate. This VYSO is associated with one of most circular and isolated ATLASGAL cores, and its light curve is also the most jittery (fluctuating), standing out from the rest.

Large-amplitude variability in YSOs can arise due to: episodic accretion events, varying extinction due to orbital motion of dusty clumps or a warped disk, or eclipsing binary or multiple sources. Spots, flares and pulsations can produce only low-amplitude variability. The non-periodic nature of the VYSO light curves rule out the possibility of eclipsing near-equal mass objects. High mass star formation is well-known to produce multiplicity, even at the formation stages (due to fragmentation), resulting in near-equal mass objects and/or several low mass objects. The light curves for the sample here are only sensitive to near-equal mass companions. Varying extinction if it occurs should reflect in an associated reddening of the source. The 13 VYSOs are included in the larger sample of Contreras Peña et al. (2016a) who have examined the reddening effects and find that it is not a dominant mechanism to reproduce the high-amplitude variability. Therefore, the most likely origin of the observed large-amplitude variability in these intermediate to high-mass VYSOs must be accretion events. Intermediate resolution near-infrared spectra for five of the VYSOs (374, 405, 406, 665, 717) have been discussed by Contreras Peña et al. (2016b). All the five sources display shocked H_2 emission at 2.12μm , irrespective of their light curve classification. Three of these sources also display Brγ in emission. Both H_2 and Brγ emission are consistent with the scenario of ongoing accretion. The case of V723 Carinae as a massive eruptive variable (Tapia, Roth & Persi 2016) published during the course of this study represents another excellent case of the variable phenomenon in massive young stars.

The analysis of the light curves showed that the most significant underlying phased signals have periods of the order of a few hundred days with a median ∼500 days. This timescale and the nature of variability found here (eruptive, dipper, LPV) are very similar to the variations of the 6.7GHz class II methanol maser emission in high mass star forming regions, both in its nature (Goedhart, Gaylard & van der Walt 2004) and in the timescales (Goedhart et al. 2014). The class II methanol masers are thought to be pumped by infrared radiation (Cragg, Sobolev & Godfrey 2005) and found to originate in accretion disks in high mass star forming regions (Sanna et al. 2010; Sugiyama et al. 2014). The similarity in the variability found in the MME and the IR variability may therefore represent the frequency of the infrared luminosity variations of the warm disk from accretion events, which is also responsible for pumping the class II MME (Cragg, Sobolev & Godfrey 2005). We searched for MME in the 13 VYSOs and did not find any methanol masers within a radius of 30″. de Villiers et al. (2015) argue that even though the onset of the 6.7 GHz MME is strongly associated with the outflow, and hence accretion activity, a critical abundance of the methanol molecule is required to produce the MME. It is therefore likely that the MME sources are younger and/or embedded in denser regions in comparison with the evolutionary states of the VYSOs studied here. Nevertheless, the common origin of both MME and IR-variability is strongly associated with the accretion phenomenon, in which case, the inferred timescale of a few hundred days may represent the timescale at which density enhancements of a spiralling disk feeds the central young star.

7. CONCLUSIONS

This study has found hitherto unknown near-infrared variability in intermediate to high-mass young stars by using the VISTA VVV data from 2010-2015. Following a stringent selection criteria to select targets with $\Delta K \geq$ 1mag, 13 VYSOs located at the peak of ATLASGAL clumps are identified. These sources are characterised by modelling their 1-850μm SEDs and by analysing their light-curves with a phase-dispersion minimisation method.

- The SED modelling of the 13 VYSO show that their luminosities are of $\sim 10^3$ $L_\odot$, the stellar masses and ages in the range of 8-11 $M_\odot$ and 10^4 - 10^6 yrs respectively.
- The light-curves are not periodic in nature. They can be classified as rising, declining or quasi-periodic. Analysis using the Plavchan method reveal that the most prominent underlying periodic signal would have an average period of ∼500days.
- The high-amplitude variability in young massive stars is attributed to episodic accretion events.

REFERENCES

Table 1. Source Details

VYSO	RA	Dec	K_s[a]	ΔK_s[b]	σK_s[c]	Light curve	Association
	deg	deg	mag	mag	mag	type[d]	
VVVv244	245.00828	-51.43392	14.4	2.08	0.59	LPV-YSO	IRDC
VVVv263	245.43405	-50.34484	13.9	2.24	0.64	Eruptive	IRDC
VVVv336	252.77721	-45.72340	14.9	2.27	0.51	Eruptive	IRDC
VVVv367	255.12338	-43.88343	14.5	2.35	0.67	Fader	IRDC
VVVv374	254.64164	-42.83201	11.7	2.41	0.73	Eruptive	IRDC, EGO, RMS[e]
VVVv389	255.82157	-42.43052	14.3	1.56	0.41	Fader	IRDC
VVVv405	257.41092	-41.64772	14.5	2.35	0.44	Dipper	HII
VVVv406	257.48944	-41.59691	13.5	2.06	0.78	Dipper	HII
VVVv665	242.49040	-50.80262	13.4	1.63	0.43	Eruptive	IRDC
VVVv717	249.02318	-46.67795	12.5	2.47	0.64	LPV-YSO	IRDC
VVVv736	252.73104	-44.11650	15.5	1.52	0.25	Dipper	IRDC
VVVv750	253.18580	-43.08889	15.8	2.73	0.82	STV	IRDC
VVVv802	258.54427	-38.50329	13.2	1.42	0.40	LPV-Mira	IRDC

[a] Average magnitudes

[b] The amplitudes for these sources are typically larger than the mean amplitudes for the 816 sample of Contreras Peña et al. (2016a), irrespective of the light curve classification.

[c] RMS variation of ΔK_s as a function of K_s for the given VVV tile

[d] LPV= long periodic variable, STV= short time scale variable

[e] RMS=Red MSX source (Lumsden et al. 2013)

Table 2. Photometric data used for SED fitting

VYSO	I1	I2	I3	I4	W3	W4	M1	PACS70	PACS160	SPIRE250	SPIRE350	SPIRE500	AGAL850
	mag	mag	mag	mag	mag	mag	mag	Jy	Jy	Jy	Jy	Jy	Jy
VVVv244	11.2	10.0	8.8	8.2	6.0	4.1	-	2.4	10.73	20.23	12.88	7.42	0.84
VVVv263	9.6	8.1	6.8	6.0	5.40	2.3[a]	1.9	3.63	17.23	-	-	-	15.0
VVVv336	11.2	9.7	8.4	7.5	-	-	4.5	-	2.31	13.47	15.87	-	3.84
VVVv367	9.8	8.3	7.0	5.8	4.6	1.9	-	6.05	5.75	7.75	-	-	4.00
VVVv374	7.4	6.5	5.6	4.8	3.9	1.7	-	40.52	35.98	65.92	40.79	25.93	3.00
VVVv389	10.0	8.7	7.9	7.3	6.2	3.6	-	0.84	5.10	12.99	15.49	38.74	13.42
VVVv405	8.8	7.4	6.0	5.1	4.4	-	2.0	7.68	40.31	89.33	31.86	71.33	7.27
VVVv406	10.2	9.3	8.5	7.6	5.6	2.5	-	3.54	26.77	41.01	-	-	10.78
VVVv665	10.0	8.9	7.8	7.0	6.3	3.8[a]	3.7	0.94	18.46	-	-	-	1.89
VVVv717	10.1	8.8	7.6	6.8	6.5	4.4[a]	4.0	0.57	2.08	-	-	-	2.45
VVVv736	10.6	9.4	8.0	7.3	5.7	2.9[a]	4.5	67.71	71.60	71.79	47.11	28.77	1.21
VVVv750	12.4	-	9.6	9.0	6.3	2.0	-	20.69	15.56	21.45	17.50	9.80	1.89
VVVv802	8.2	6.5	5.4	4.7	4.2	1.7	-	31.11	13.97	20.31	14.87	14.10	3.71

[a] not used

Table 3. SED Fitting results

VYSO	M_* $M_\odot$	$A_{V,core}$ mag	$A_{V,int}$ mag	$\dot{M}_{env}$ $10^{-5} M_\odot$ yr^{-1}	$\dot{M}_{disc}$ $10^{-6} M_\odot$ yr^{-1}	$\log Age$ yr	distance kpc	$\log L_{tot}$ $L_\odot$	χ^2_{best}/N_{data}	N_{fits}	N_{fits2}[a]
$VVVv244$	5.9 ± 2.6	192 ± 4009	32 ± 13	7.6 ± 26.2	1.1 ± 6.0	6.2 ± 0.8	5.5 ± 3.5	2.8 ± 0.7	0.05	10000	1392
$VVVv263$	8.5 ± 2.8	97 ± 595	48 ± 7	3.3 ± 3.5	3.8 ± 27.0	6.2 ± 0.7	4.2 ± 2.6	3.5 ± 0.5	0.65	684	49
$VVVv336$	7.3 ± 2.9	206 ± 2951	43 ± 9	0.0 ± 0.0	0.7 ± 2.8	6.4 ± 0.2	5.7 ± 3.3	3.2 ± 0.6	0.09	3333	8
$VVVv367$	8.3 ± 3.7	641 ± 3857	31 ± 14	3.8 ± 4.2	8.7 ± 34.0	5.7 ± 1.2	4.9 ± 2.9	3.3 ± 0.6	0.16	1035	363
$VVVv374$	8.8 ± 2.7	121 ± 1480	15 ± 4	1.6 ± 7.9	0.6 ± 4.2	6.3 ± 0.2	4.4 ± 2.5	3.5 ± 0.4	0.14	1659	113
$VVVv389$	7.3 ± 2.5	67 ± 1185	37 ± 9	0.4 ± 0.9	0.7 ± 3.1	6.4 ± 0.3	5.1 ± 3.1	3.2 ± 0.5	0.38	3200	75
$VVVv405$	11.1 ± 3.3	340 ± 3631	45 ± 6	0.0 ± 0.0	1.8 ± 6.3	6.3 ± 0.2	4.4 ± 2.3	3.8 ± 0.4	0.64	806	0
$VVVv406$	5.3 ± 2.5	83 ± 3391	13 ± 11	2.8 ± 3.2	2.8 ± 8.7	4.9 ± 0.9	5.7 ± 3.6	2.6 ± 0.7	0.25	3172	2812
$VVVv665$	7.6 ± 2.5	69 ± 1056	37 ± 8	0.0 ± 0.2	0.7 ± 2.7	6.4 ± 0.2	5.5 ± 3.2	3.3 ± 0.5	0.03	3969	51
$VVVv717$	8.5 ± 2.8	73 ± 691	44 ± 6	0.0 ± 0.0	1.5 ± 4.1	6.3 ± 0.2	5.7 ± 3.3	3.5 ± 0.5	0.49	1459	0
$VVVv736$	7.5 ± 2.9	224 ± 3415	36 ± 12	58.8 ± 96.1	0.5 ± 3.5	6.4 ± 0.3	5.9 ± 3.3	3.2 ± 0.6	0.0	5515	204
$VVVv750$	7.4 ± 3.3	450716 ± 5232901	11 ± 8	15.8 ± 17.0	19.8 ± 71.2	4.1 ± 0.7	6.2 ± 3.8	2.9 ± 0.6	0.08	1807	1806
$VVVv802$	11.5 ± 3.2	160 ± 2169	47 ± 5	0.9 ± 1.7	2.3 ± 10.0	6.3 ± 0.2	3.5 ± 1.6	3.9 ± 0.4	0.29	1635	5

[a]The number of models with a non-zero envelope accretion rate.

Table 4. Light curve analysis results

VYSO	Per1[a]	Pwr1[b]	Per2	Pwr2	Per3	Pwr3
VVVv244	107.7	28.5	809.0	26.0	7.0	24.7
VVVv263	314.0	122.7	560.0	54.3	-	-
VVVv336	886.3	20.8	283.5	20.1	327.1	9.5
VVVv367	289.7	14.8	146.9	10.7	114.0	8.5
VVVv374	454.0	59.1	251.3	22.4	124.3	12.1
VVVv389	188.5	12.2	233.1	12.2	438.7	11.5
VVVv405	491.5	12.4	231.1	6.5	113.4	6.5
VVVv406	491.9	227.1	939.0	66.6	-	-
VVVv665	834.7	23.1	303.9	7.2	-	-
VVVv717	851.0	177.8	277.4	68.8	-	-
VVVv736	493.1	18.8	311.5	13.3	235.6	9.5
VVVv750	66.2	183.9	44.4	169.2	-	-
VVVv802	631.4	326.7	890.7	165.4	-	-

[a] Period in days

[b] Power of Per1

NOTE—Sources with missing p3 display relatively clean power spectrum with two significant periods of probability statistics p-value=0

Audard, M., Abraham, P., Dunham, M. M. et al. 2014, in Protostars and Planets VI, eds. Beuther, H., Klessen, R. S., Dullemond, C. P., & Henning, T., University of Arizona Press, Tucson, p387

Bernasconi, P. A., & Maeder, A. 1996, A&A, 307, 829

Bouvier, J., Alencar, S. H. P., Harries, T. J., Johns-Krull, C. M., & Romanova, M. M. 2007, in Protostars & Planets V, B. Reipurth, D. Jewitt, and K. Keil (eds.), University of Arizona Press, Tucson, 951pp., 2007., p. 479-494

Bouvier, J., & Bertout, C. 1989, A&A, 211, 99

Carey, S. J., Noriega-Crespo, A., Mizuno, D. R., et al. 2009, PASP. 121, 76

Carpenter, J. M., Hillenbrand, L. A., & Skrutskie, M. E. 2001, AJ, 121, 3160

Cesaroni, R., Galli, D., Lodato, G., Walmsley, C. M. & Zhang, Q. 2007, in Protostars and Planets V, Eds. B. Reipurth, D. Jewitt & K. Keil, University of Arizona Press, Tucson, 951, p.197

Churchwell, E., Babler, B. L., Meade, M. R., et al. 2009, PASP, 121, 213

Contreras, C., Lucas, P. W., Minniti, D., Kurtev, R., Stimson, W. et al. 2016a, MNRAS, submitted, arXiv:1602.06267

Contreras, C., Lucas, P. W., Minniti, D., Kurtev, R., Stimson, W. et al. 2016b, MNRAS, submitted, arXiv:1602.06269

Cragg, D. M., Sobolev, A. M. & Godfrey, P. D. 2005, MNRAS, 360, 533

Cyganowski, C. J., Whitney, B. A., Holden, E., et al. 2008, AJ, 136, 2391

de Villiers, H. M., Chrysostomou, A., Thompson, M. A., et al. 2015, MNRAS, 449, 119

Faesi, C. M., Covey, K. R., Gutermuth, R., Morales-Calderon, M., Stauffer et al. 2012, PASP, 124, 1137

Fernandez, M. & Eiroa, C. 1996, A&A, 310, 143

Goedhart, S., Gaylard, M. J. & van der Walt, D. J. 2004, MNRAS, 355, 553

Goedhart, S., Maswanganye, J. P., Gaylard, M. J. & van der Walt, D. J. 2014, MNRAS, 437, 1808

Grave, J. M. C., & Kumar. M. S. N. 2009, A&A, 498, 147

Hartmann, L., Kenyon, S. J., & Calvet, N. 1993, ApJ, 407, 219

Hayashi, C. 1966, ARA&A, 4, 171

Herbst, W., & Shevchenko, V. S. 1999, AJ, 118, 1043

Iben, I. 1965, ApJ, 141, 993

Jackson, J. M., Susanna, C., Rathborne, J. M., Chambers, E. T., & Simon, R. 2008, ApJ, 680, 349

Kallinger, T., Zwintz, K., & Weiss, W. 2008, A&A, 488, 279

Kumar, M. S. N. & Grave, J. M. C. 2007, A&A, 462, 37

Krumholz, M. R., Klein, R. I., McKee, C. F., Offner, S. R. & Cunningham, A. J. 2009, Science, 323, 754

Lada, C. J., & Adams, F. C. 1992, ApJ, 393, 278

Lumsden, S., Hoare, M. G., Urquhart, J. S., et al. 2013, ApJS, 208, 11

Minniti D., et al. 2010, NewA, 15, 433

Molinari, S., Swinyard, B., Bally, J., et al. 2010, PASP, 122, 314

Peretto, N., & Fuller, G. A. 2009, A&A, 505, 405

Plavchan, P., Kirkpatrick, J. D., Cutri, R. M. & Gallagher, S. C. 2008, ApJS, 175, 191

Robitaille, T. P., Whitney, B. A., Indebetouw, R., Wood, K., & Denzmore, P. 2006, ApJS, 167, 256

Robitaille, T. P., Whitney, B. A., Indebetouw, R. & Wood, K. 2007, ApJS, 169, 328

Robitaille, T. P., Meade, M. R., Babler, B. L., Whitney, B. A., Johnston, K. G. et al. 2008, AJ, 136, 2413

Sanna, A., Moscadelli, L., Cesaroni, R., Tarchi, A., Furuya, R. S., & Goddi, C. 2010, A&A, 517, 78

Schuller, F., Menten, K. M., Contreras, Y., Wyrowski, F., Schilke, P. et al. 2009, A&A, 504, 415

Sugiyama, K., Fujisawa, K., Doi, A., Honma, M., Kobayashi, H., et al. 2014, A&A, 562, 82

Tapia, M., Roth, M., & Persi, P. 2015, MNRAS, 446, 4088

Wolk, S. J., Günther, H. M., Poppenhaeger, K., et al. 2015, AJ, 150, 145